Journal of Applied Physics

RESEARCH ARTICLE | JULY 03 2025

Development of complex-modeling with Fourier transform (CFT) for ultrafast simulation of transient energy transport

Yu Hua ; Ibrahim Al Keyyam ; Yangsu Xie ; Xinwei Wang

J. Appl. Phys. 138, 015104 (2025)
https://doi.org/10.1063/5.0275419
CHORUS

Journal of Applied Physics METHOD pubs.aip.org/aip/jap

Development of complex-modeling with Fourier transform (CFT) for ultrafast simulation of transient energy transport

Cite as: J. Appl. Phys. **138**, 015104 (2025); doi: 10.1063/5.0275419
Submitted: 12 April 2025 · Accepted: 14 June 2025 ·
Published Online: 3 July 2025

Yu Hua,[1] Ibrahim Al Keyyam,[1] Yangsu Xie,[2] and Xinwei Wang[1,a)]

AFFILIATIONS

[1]Department of Mechanical Engineering, Iowa State University, Ames, Iowa 50011, USA
[2]College of Chemistry and Environmental Engineering, Shenzhen University, Shenzhen, Guangdong 518055, People's Republic of China

[a)]**Author to whom correspondence should be addressed:** xwang3@iastate.edu. **Tel.:** 001-515-294-8023.

ABSTRACT

Solving transient energy transport is crucial for accurately predicting the behavior of materials and devices during thermal cycling, pulsed heating, and transient operational states where heat generation and dissipation rates vary over time. Traditional methods, like the finite difference and element methods, discretize space and time and update temperature values at each grid point iteratively over time steps. Its straightforward implementation makes it popular for solving heat transfer problems. However, when high temporal and spatial resolutions or prolonged heating durations are required, the computational demand rises significantly, leading to significantly greater resource consumption. To address this, in this work we develop a new method termed Complex-modeling with Fourier Transform (CFT) that enables rapid and efficient simulations of transient energy transport problems. The CFT method decomposes the periodical heating problem into a complex-temperature energy transport problem with a single harmonic heat source. 1D and 3D transient heat conduction problems (conjugated with hot carrier transfer) are solved using the CFT method to demonstrate its effectiveness. The CFT method produces similar or higher accuracy results compared with the finite difference method, while the computational speed is increased by more than two orders of magnitude. We also developed a new method termed Complex-modeling with Fourier and Heaviside Transforms (CFHT) that can solve any transient energy transport problems with orders of magnitude speed increase. The CFT and CFHT methods developed in this work are applicable to linear problems that could involve mechanical, thermal, optical, and electrical responses.

I. INTRODUCTION

Transient energy transport phenomena are prevalent in numerous engineering problems, e.g., transient response of computer chips during the start-up stage or under sudden load change, and rechargeable batteries during charge and discharge states. One critical category of transient energy transport is a system's response under periodical thermal loading (e.g., laser heating or Joule heating). Such periodical heating is commonly used in thermophysical properties characterization. One good example is the photothermal (PT) technique that involves heating the sample surface with a periodically amplitude-modulated laser beam and probing the periodical surface response via measuring surface laser reflection, thermal radiation, or acoustic response of the adjacent air.[1–3] If the laser beam size is much larger than the thermal diffusion length during one heating period, the heat transfer problem can be treated as one-dimensional and an analytical solution has been developed for the sample's thermal response with consideration of the laser volumetric absorption and interfacial thermal resistance (R''_{tc}).[3–5] However, if the heat transfer diffusion length is much longer than the laser beam size, 3D heat transfer has to be considered. Analytical solution development for such scenarios becomes much more challenging and difficult. Solutions can be developed using Green's function method[6] with neglected physics (e.g., interfacial thermal resistance and anisotropic thermal

conductivity of materials). Still, the integral of the Green's function to obtain the temperature field is very time consuming.

For more complicated cases that involve periodical heating of a heterogenous system, numerical modeling has to be used to solve for the sample's thermal response. For instance, in the frequency-domain energy transport-state resolved Raman (FET-Raman) technique, a nm-thick 2D material is supported on a substrate. A square-wave modulated laser beam is used to heat the sample, and the Raman signal is collected at the same time.[7,8] For this type of situation, 3D numerical modeling has to be used to fully consider the very fine thickness of the 2D material and the large size of the substrate. Even using spatially varying meshes, the computation itself is still very expensive since the modeling has to be conducted for a long time until the sample's surface reaches a quasi-steady state when the temperature field changes with time periodically and no further temperature accumulation is observed. Using a modern lab PC, such computation usually takes about 10 h or more, depending on the complexity of the problem itself.[9] Also, this modeling needs to be high-precision since it is used to fit the experimental data to determine properties like thermal conductivity (κ), R''_{tc}, and hot carrier diffusivity (D). This is especially time consuming when scanning a 3D space of κ, R''_{tc}, and D to identify the right combination if the three properties are determined simultaneously. For instance, 10 values of each property will generate a scanning of 1000 property combinations for data fitting while keeping high accuracy of modeling. This has implemented significant hurdles in measuring the thermophysical properties of 2D materials.

In this work, first we present a novel 3D numerical modeling method, termed Complex-modeling with Fourier Transform (CFT) to tackle the above problem. The CFT method decomposes the periodical heating problem into distinct problems with single-frequency harmonic heating, solves them in the complex domain, and reconstructs the solution in the physics field. Then, examples of heat transfer in a supported nm-thick bundle of single-walled carbon nanotubes (SWCNTs) and supported 2D materials are used to demonstrate the effectiveness and accuracy of the new method. Finally, a general and universal Complex-modeling with Fourier and Heaviside Transform (CFHT) is presented for transient thermal transport problems of arbitrary heating that still features the same modeling effectiveness and accuracy.

II. THE CFT METHOD: PHYSICS AND PRINCIPLES

The CFT method developed in this work is applicable to all linear heat transfer problems. Here, we take a general heat conduction problem with a periodical heating source described by the below equation

$$\rho c_p \frac{\partial T}{\partial t} = \nabla(\kappa_i \nabla T) + g(\vec{r}) \cdot \dot{q}(t), \tag{1}$$

where ρ is density, c_p specific heat, k thermal conductivity, T temperature, and $g(\vec{r}) \cdot \dot{q}$ the heat source term. Here, $g(\vec{r})$ describes the heat source distribution in space and $\dot{q}(t)$ describes the temporal variation of the heat source and is independent of location. Note to make the equation linear, all the thermophysical properties are assumed temperature independent. This is physically reasonable for moderate temperature rise problems. Here, $\dot{q}$ periodically varies with time with a frequency f and is the same in the heating region, but takes an arbitrary form. Here, we are interested in the temperature field when the system reaches the quasi-steady state: the temperature varies with time periodically and no further temperature accumulation occurs. For such a scenario, the temperature consists of two components as $T = T_s + T_t$, where T_s is the steady-state component which could have a distribution in space, but not change with time, and T_t is the part varying with time periodically.

Traditional numerical modeling of this problem using the finite difference or element method simulates the problem from the initial condition step by step and continues until it reaches the quasi-steady state. This usually needs to simulate a significantly long time of heat transfer in the order of L^2/α, where L is the domain characteristic size, and α is the domain's thermal diffusivity. Here, we decompose the problem to ones with single harmonic periodical heating that can be solved in the complex space just one time, and then the solution of the original problem can be constructed based on the solutions of these single harmonic periodical heating problems. We term this method as Complex-modeling with Fourier Transform (CFT), and it can be applied to all finite numerical modeling methods. At present, the description and examples are restricted to the situation that $\dot{q}$ follows the same form of variation with time in the heating region. Generalization of this method will be discussed later.

The term $\dot{q}(t)$ can be expressed using the Fourier transform as

$$\dot{q} = a_0 + \sum_{n=1}^{\infty} [a_n \cos(\omega_n t) + b_n \sin(\omega_n t)], \tag{2}$$

where $\omega_n = n2\pi f$. Since the problem described by Eq. (1) is a linear problem because the thermophysical properties are taken as temperature independent, the temperature field induced by $\dot{q}$ can be expressed as a sum of the temperature rises caused by heating sources of a_0, $a_n\cos(\omega_n t)$, and $b_n\sin(\omega_n t)$ as

$$T_t(\vec{r}, t) = T_0 + \sum_{n=1}^{\infty} [T_{n,a} + T_{n,b}]. \tag{3}$$

The temperature rise (T_0) caused by a_0 represents a steady problem and can be readily solved. To find the temperature rises $T_{n,a}$ and $T_{n,b}$, respectively, caused by $a_n\cos(\omega_n t)$ and $b_n\sin(\omega_n t)$, we consider a case of the problem under single-frequency harmonic periodical heating with the same spatial heat source distribution $g(\vec{r})$. The governing equation is expressed in the complex domain as

$$\rho c_p \frac{\partial T_n}{\partial t} = \nabla(\kappa_i \nabla T_n) + g(\vec{r}) e^{i\omega_n t}. \tag{4}$$

For this problem, the temperature can be expressed as $T_n = \theta_n e^{i\omega_n t}$. The situation of $n = 0$ is for the case of steady-state temperature, and the solution θ_0 will be T_s mentioned above. With this form of T_n, the heat transfer governing equation is simplified as

$$\rho c_p i\omega_n \theta_n = \nabla(\kappa_i \nabla \theta_n) + g(\vec{r}). \tag{5}$$

This represents a 3D steady-state problem that can be solved numerically using the finite difference or element method. Note this problem needs to be solved in the complex space, meaning θ_n will be a complex number. After θ_n is solved, it is readily realized that the temperature field caused by $a_n\cos(\omega_n t)$ is $T_{n,a} = a_n \mathrm{Re}[\theta_n(\vec{r})e^{i\omega_n t}]$, the temperature field caused by $T_{n,b} = b_n\sin(\omega_n t)$ is $b_n \mathrm{Im}[\theta_n(\vec{r})e^{i\omega_n t}]$, and the temperature field caused by a_0 is $T_0 = a_0\theta_0(\vec{r})$. Finally, the solution to the problem described by Eq. (1) can be reconstructed as

$$T(\vec{r}, t) = a_0\theta_0(\vec{r}) + \sum_{n=1}^{\infty}\left\{a_n \mathrm{Re}\left[\theta_n(\vec{r})e^{i\omega_n t}\right] + b_n \mathrm{Im}\left[\theta_n(\vec{r})e^{i\omega_n t}\right]\right\}. \quad (6)$$

Note for the Fourier transform of Eq. (2), the needed terms to capture the $\dot{q}$ variation with time depend on the complexity of its form. However, as we will show later, generally speaking, 40 terms will be sufficient with the help of Heaviside Transform. Since a heat transfer problem can involve very different boundary conditions, these should be carefully considered and implemented when solving Eqs. (4) and (5). Here, we provide some discussions to illustrate, which should not be treated exclusive. For a constant temperature boundary condition of Eq. (1), this should be implemented in the case of $n = 0$ for Eq. (4), while for $n \geq 1$ the boundary condition should be zero temperature rise. Adiabatic boundary conditions of Eq. (1) should be applied to all situations of Eq. (4).

III. HEAT TRANSFER IN A SUPPORTED NM-THICK SWCNT BUNDLE

The heat dissipation in microelectronics is often hindered by a special type of resistance known as interfacial thermal resistance (or thermal boundary resistance). Thermal interface materials (TIMs) like carbon nanotubes (CNTs) are often used to enhance heat dissipation due to their exceptional thermophysical and mechanical properties.[10] Therefore, studying the heat transfer when CNTs are in contact with different substrates is essential for optimizing future electronic performance and better understanding the fundamental physics. Extensive research has focused on experimentally investigating the thermal properties of CNTs and other carbon-based materials.[11] In any typical measurement, the goal is to experimentally establish a relationship between various heat currents (electrical, optical, etc.) and the sample's thermal response to infer thermophysical properties. This is usually done by solving the heat transfer equation numerically as analytical solutions are often unavailable. The properties of interest can then be extracted from the solution of the heat transfer equation by mapping out the experimental findings. Therefore, developing ultrafast and accurate numerical methods for transient energy transport is very critical.

Traditional methods, like the finite difference (FD) method discretize space and time, updating temperature values at each grid point iteratively over time steps. Its straightforward implementation makes it popular for solving heat transfer problems. However, when a fine temporal resolution or a long heating time is required, the computational demand rises significantly, leading to a higher resource usage. In this section, we resolve this issue using the CFT method detailed above to demonstrate its great accuracy and effectiveness.

In the following analysis, we use the FD and CFT methods to simulate the energy transport in supported samples under periodic laser heating and compare their results. This is a common problem that mimics the heat transfer in nano-resolved Raman thermometry like the frequency-domain energy transport state-resolved Raman (FET-Raman).[8] The FET-Raman is commonly used to measure thermal conductivity and interfacial thermal conductance with high accuracy. Figure 1 illustrates a schematic of the heat transfer problem under consideration in FET-Raman to measure a supported SWCNT bundle. An amplitude-modulated laser beam irradiates the SWCNT bundle to induce heating. At the same time, this laser also excites Raman signals, which are collected and used to probe the sample's temperature response.

The one-dimensional heat transfer model for the problem illustrated in Fig. 1 can be expressed as[12–14]

$$\kappa\frac{\partial^2 T}{\partial x^2} - \frac{T - T_s}{R' \cdot A_c} + \dot{q} = \rho c\frac{\partial T}{\partial t}. \quad (7)$$

Here, R' is the interfacial thermal resistance (per unit length) between the sample and substrate sustained by interfacial phonons,[15] T_s is the temperature of the substrate surface, and A_c is the solid cross-sectional area of the bundle. The volumetric heat source term ($\dot{q}$) that mimics the laser heating is represented by a Gaussian profile and defined as

$$\dot{q}(x, t) = \dot{q}_0\exp\left[-(x - x_0)^2/r_0^2\right] \cdot \Psi, \quad (8)$$

where $\dot{q}_0$ is the peak heat source at the center of the laser beam ($x = 0$), r_0 is the radius of the laser beam which depends on the objective lens used, x_0 is the location of the laser beam center, and $\Psi(t)$ is the temporal modulation of the laser beam to produce a square-wave function. The square wave with a 50% duty cycle can be expressed using a Fourier series as $\Psi(t) = 0.5 + 4/\pi \cdot \sum_{n=1}^{\infty}\sin[(2n-1)\omega t/(2n-1)]$. The series can be truncated earlier to ensure computational efficiency while maintaining high accuracy, as shown in Fig. 2(a).

For the SWCNT bundle studied here, since its length (10 μm) is much longer than the laser heating area and thermal diffusion length, its ends are assumed to maintain their initial temperature, unaffected by the laser heating. In the following analysis, 40 Fourier terms are used by default in the CFT method, unless specified otherwise. In the FD method, the time step is set to 1 ps. For both methods, the 10 μm spatial domain is divided into uniform 3000 grids. The laser spot radius (r_0) is set to 0.8 μm, unless specified otherwise, and the simulations are carried out per 1 mW effective absorbed laser energy. The thermal conductivity of SWCNT is highly dependent on the defect level within the sample and ranges from 10s to 100s W m^{-1} K^{-1} at room temperature as revealed by various experimental and computational methods reported in literatures.[16–18] In our simulations, we pick an intermediate value of 330 W m^{-1} K^{-1}. The room-temperature interfacial thermal resistance, on the other hand, has been measured to be from 100s to

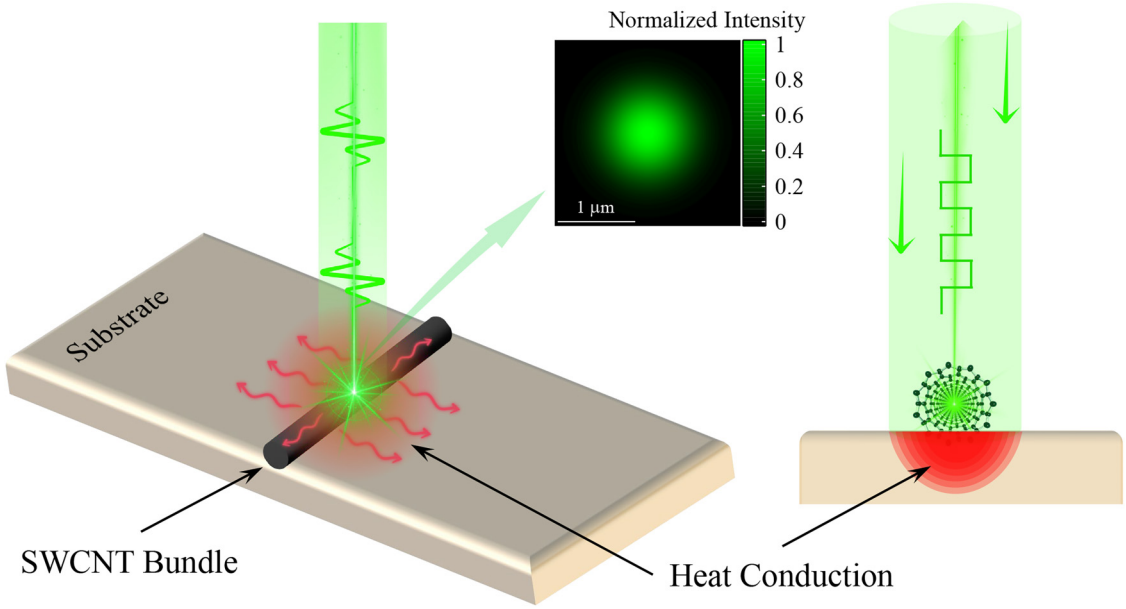

FIG. 1. Schematic of a supported SWCNT bundle under periodic laser heating. Heat is conducted along the SWCNT bundle through in-plane phonons and into the substrate through interfacial phonons. The inset shows the spatial variation of laser intensity under a 50× objective.

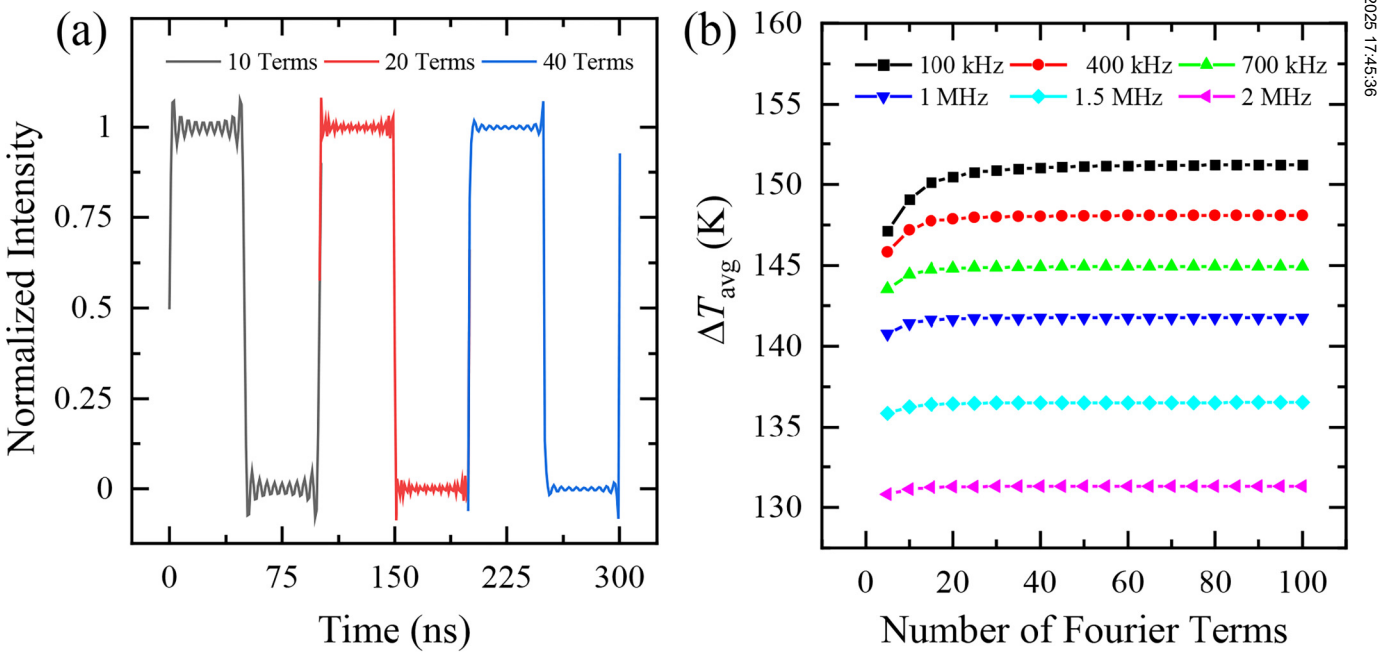

FIG. 2. (a) Reconstruction of the square-wave laser using different numbers of Fourier terms. (b) The Raman intensity-weighted average temperature rise as a function of the number of Fourier terms for different laser frequencies under 50× objective.

1000 K m W^{-1}.[12,14,19] We emphasize that the specific choice of input parameters will have no impact on the conclusions drawn from this work, providing that the two simulation methods are carried out under the same set of parameters. The input parameters used in the following case study are summarized in Table I.

Figure 2(a) shows the reconstruction of the square wave laser beam based on a different number of terms in Fourier transform. It is evident that the least number of Fourier terms needed to effectively reconstruct the square laser pulse is about 40. The oscillations at the beginning and end of the duty will have a negligible effect on the temperature field since the oscillations have a small amplitude, existing for a very short time compared with the laser-on time, and the oscillation itself has near-zero accumulation. Figure 2(b) shows the impact of the number of Fourier terms on the Raman intensity-weighted average temperature rise (ΔT_{avg}) under the laser spot for different laser modulation frequencies. The temperature rise is weighted over the laser spot area as $\Delta T_{avg} = \int_0^{x_0} I\Delta T \cdot dx / \int_0^{x_0} I dx$, where I is the intensity of the laser that varies spatially, as shown in Fig. 1, and takes the form $I = I_0 \exp[-(x - x_0)^2/r_0^2]$. This averaging is essential when interpreting the results of nano-resolved Raman thermometry experiments like the FET-Raman simulated here. The results in Fig. 2(b) firmly confirm that 40 terms are sufficient for ΔT_{avg} to converge to a quasi-steady-state value.

We find that the higher the modulation frequency, the lower the quasi-steady-state temperature rise and the lower the number of Fourier terms needed for the response to converge, as clearly seen in Fig. 2(b). The observations can be explained by the fact that under extremely high-frequency modulation, the temperature rise during the excitation period and the temperature drop during the thermal relaxation period are minimal and nearly negligible. Consequently, the sample maintains an almost constant quasi-steady-state temperature throughout the process. In the limit of infinitely high frequency, this quasi-steady-state temperature equals half of that under steady-state heating since the sample is subjected to half of the continuous wave (CW) laser incident energy. This result has been detailed in a former study.[21] Therefore, at high frequencies, the rise in temperature can be effectively captured by the DC component (a_0) to a large extent. Hence, a smaller number of Fourier terms is enough. As the frequency gets lower, the quasi-steady-state temperature starts to increase. For a sufficiently low frequency, it eventually approaches the steady-state temperature under a CW laser heating, which requires more Fourier terms to capture the response. Nevertheless, even for the lower frequency end (100 kHz) shown in Fig. 2(b), the temperature seems to have very little more room to increase before convergence, and the difference between the temperature using 40 terms and the quasi-steady-state temperature is less than 0.3%. This further confirms that using 40 terms in the Fourier transform suffices to obtain reliable and accurate results. It is worth noting that the classification of frequencies as high or low is strongly influenced by the thermophysical properties and the size of the sample under consideration.

TABLE I. Input parameters for the case study.

Parameter	Value	Units
Length of the SWCNT bundle	10	μm
Diameter of the SWCNT bundle	28.2	nm
Solid cross-sectional area of the SWCNT bundle	624.6	nm^2
Thermal conductivity[16–18]	330	W m^{-1} K^{-1}
Interfacial thermal resistance[13]	500	K m W^{-1}
Volumetric heat capacity[16,20]	1.36×10^6	J m^{-3} K^{-1}
Laser spot radius	0.4–1.8	μm
Frequency of the square-wave modulated laser	0.1–10	MHz
Number of frequency components in Fourier transform	40	…
Spatial grid size	3.33	nm
Time step in the FD method	1	ps

The temperature field in the entire SWCNT bundle is plotted in Figs. 3(a) and 3(b). We find nearly identical results by the two methods, despite the tremendous reduction in the computational head by the CFT method. The largest temperature rise (157 K) is at the center of the Gaussian beam where the intensity is maximum. We further extract the temperature evolution at three different locations within the bundle marked in dashed/solid lines in Figs. 3(a) and 3(b). The results as shown in Fig. 3(c) are very consistent where both methods yield almost identical temperature rises. To quantify the discrepancies between them, the relative difference defined as $(\Delta T_{FD} - \Delta T_{CFT})/\Delta T_{CFT}$ is plotted in Fig. 3(d). The results show a difference of less than 3% between the two methods. The maximum difference is observed at the very beginning of the heating cycle, which is attributed to the oscillation of the reconstructed square-wave laser pulse at the beginning [Fig. 2(a)]. However, this has a negligible effect on the temperature evolution of further time and quickly dies out and converges to a value of less than 0.1%. The relative difference is observed to be smaller for locations closer to the laser heating source. Hence, for applications where the average temperature rise is desired, such as the Raman-probed temperature rise under the laser spot, the difference is further diminished as shown in Fig. 4(b) since the differences are averaged out spatially over the heating region and heating time.

The laser heating size is a crucial parameter that is often used to construct different energy transport states and provides the capability to conduct simultaneous measurement of different physical properties such as thermal conductivity, interfacial thermal conductance, and more.[12] To study the heating size's impact on the thermal transport problem using the two methods, the simulation is carried out for three different objective lens that are commonly used in nano-resolved Raman measurements: 20×, 50×, and 100×, which correspond to a laser spot radius (r_0) of 1.8, 0.8, and 0.4 μm, respectively. The results for the Raman intensity-weighted average temperature rise as a function of the pulse period are shown in Fig. 4(a), where the output is nearly identical. The temperature rise under the 100× is shown to be the largest since the laser energy is confined to a smaller area. As discussed earlier, lower frequencies which correspond to longer pulse periods ($1/f$) yield higher average temperature rise as longer periods allow more thermal accumulation and temperature build-up. The relative difference between the

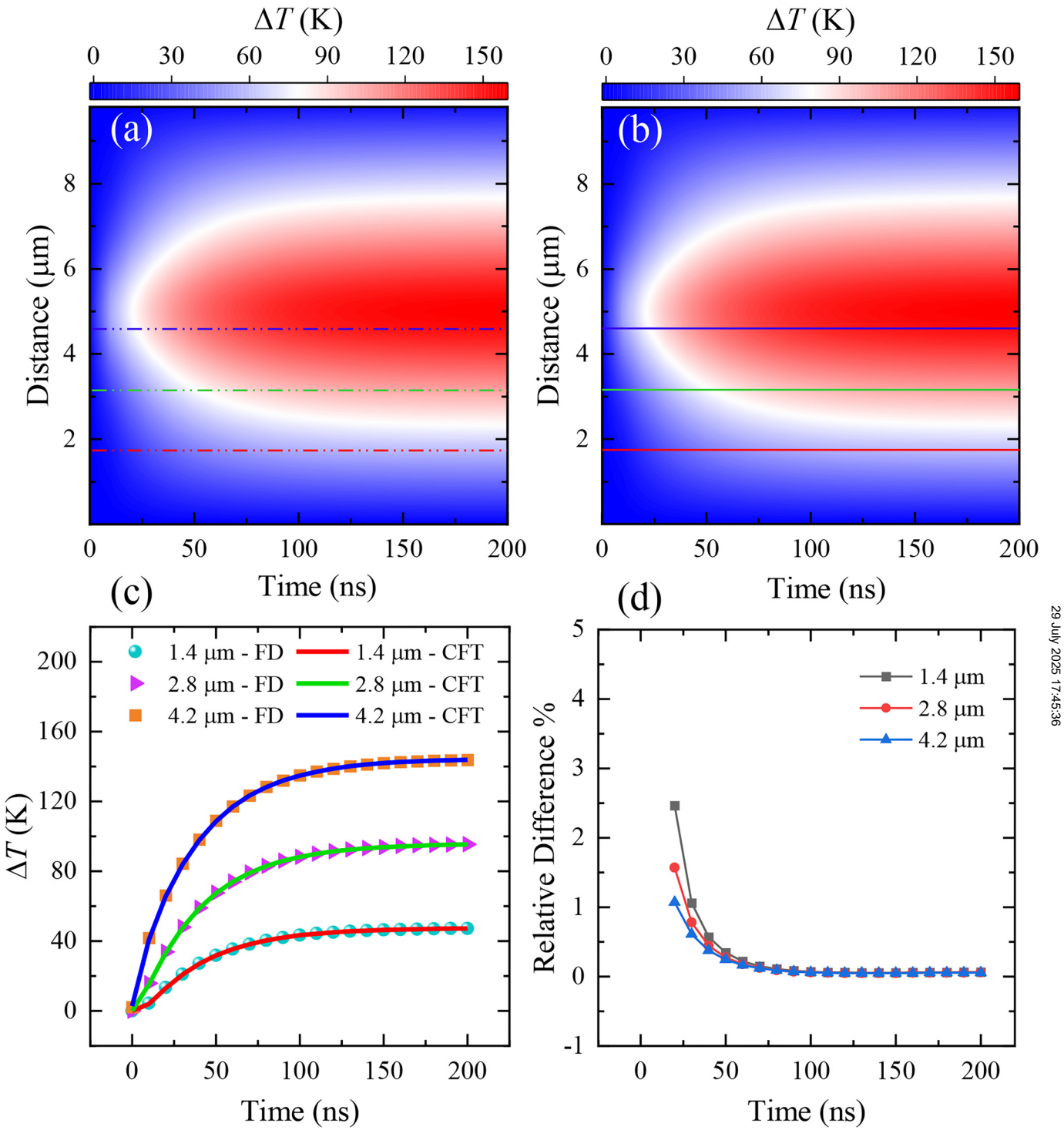

FIG. 3. The temperature contour in the spatial and temporal domains using (a) the finite difference method and (b) the Complex-modeling with Fourier Transform (CFT) method. The y coordinate is for the distance from the laser beam center. The horizontal dashed/solid lines correspond to the specific locations inspected for the temperature evolution. (c) Comparison of the temperature evolution using the two methods at different locations. (d) The relative difference between the two methods as a function of time at different locations. The frequency of the laser modulation is set to 1 MHz.

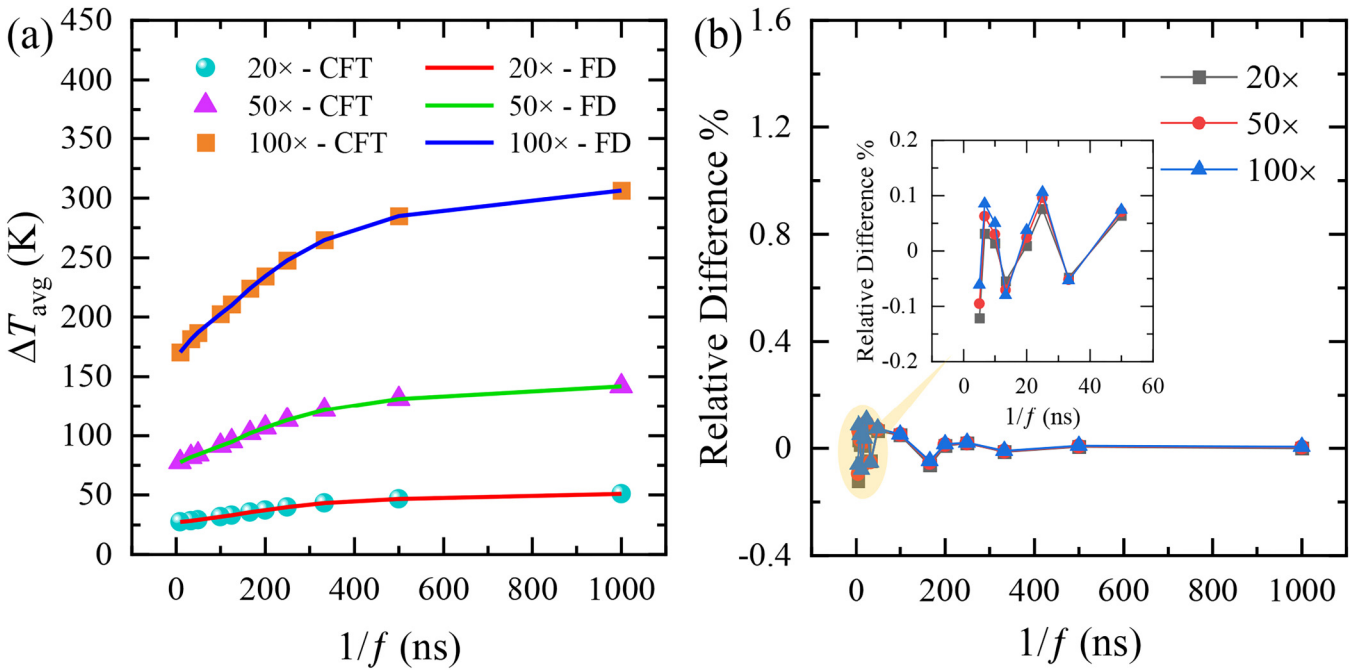

FIG. 4. (a) The Raman intensity-weighted average temperature rise under the laser spot using the two methods as a function of the heating pulse period under different objective lens. (b) The relative difference between the two methods as a function of the heating pulse period and different objective lens.

two methods is shown to be less than 0.2% for the studied range of laser pulse periods, as illustrated in Fig. 4(b).

In the previous case study, both the FD and CFT methods aim to predict temperature distribution and evolution in a supported SWCNT bundle subjected to localized periodic laser heating. While both use similar spatial discretization, their computational costs scale differently based on temporal and frequency considerations. The computational cost of the FD method primarily depends on the total time required for the temperature to converge to a quasi-steady-state value which itself depends on the temporal resolution. Smaller pulse widths often demand finer resolutions and require simulating multiple heating cycles for temperature convergence. To give a quantitative example, if the total time needed for convergence is 1 μs with a 0.1 ns time step, the heat conduction equation must be solved 10 000 times in the FD method. In contrast, the CFT method's cost scales with the number of frequency components used in the Fourier transform. As shown in Fig. 2, only 40 Fourier terms are sufficient for the temperature to converge to a quasi-steady-state value, meaning that the heat conduction equation is solved only 40 times. Therefore, the CFT method is more than two orders of magnitude faster than the FD method under these conditions. This reduction in computational head can far exceed this as shown in Sec. IV. While the FD method provides real temperature values directly as a function of space and time, the CFT method produces complex values as a function of space and frequency, requiring an additional transformation to the time domain. Nevertheless, the CFT method's efficiency and significantly reduced computational burden makes it superior, particularly for scenarios demanding a high temporal resolution in computation.

IV. CONJUGATED PHONON AND HOT CARRIER TRANSPORT IN SUPPORTED 2D MATERIALS

In this section, we demonstrate solving conjugated heat conduction and hot carrier diffusion in 3D processes using the CFT technique. These processes are involved in 2D materials under laser heating that is involved in thermal characterization using Raman spectroscopy. Raman spectroscopy has significantly advanced the study of thermal properties of 2D materials.[22] However, conventional Raman methods face notable limitations in accuracy, particularly when dealing with complex heat transfer scenarios.[9] The challenges stem from the assumptions in traditional physical frameworks, which roughly evaluate critical factors such as laser absorption[23] and temperature coefficient of Raman parameters, and neglect the heating area extension caused by hot carriers diffusion.[24] As a result, discrepancies between experimental results and theoretical predictions often arise, hindering in-depth physics understanding of energy transport in 2D materials.

To address these challenges, our FET-Raman methodology[25] was developed for thermal properties measurement of 2D materials. As shown in Fig. 5 for a 2D material supported on a substrate, two energy transport states are constructed under laser heating: a steady state from CW laser heating and a transient state from amplitude-modulated laser heating. It should be noted that although the two states have different optic field distribution in time domain, their

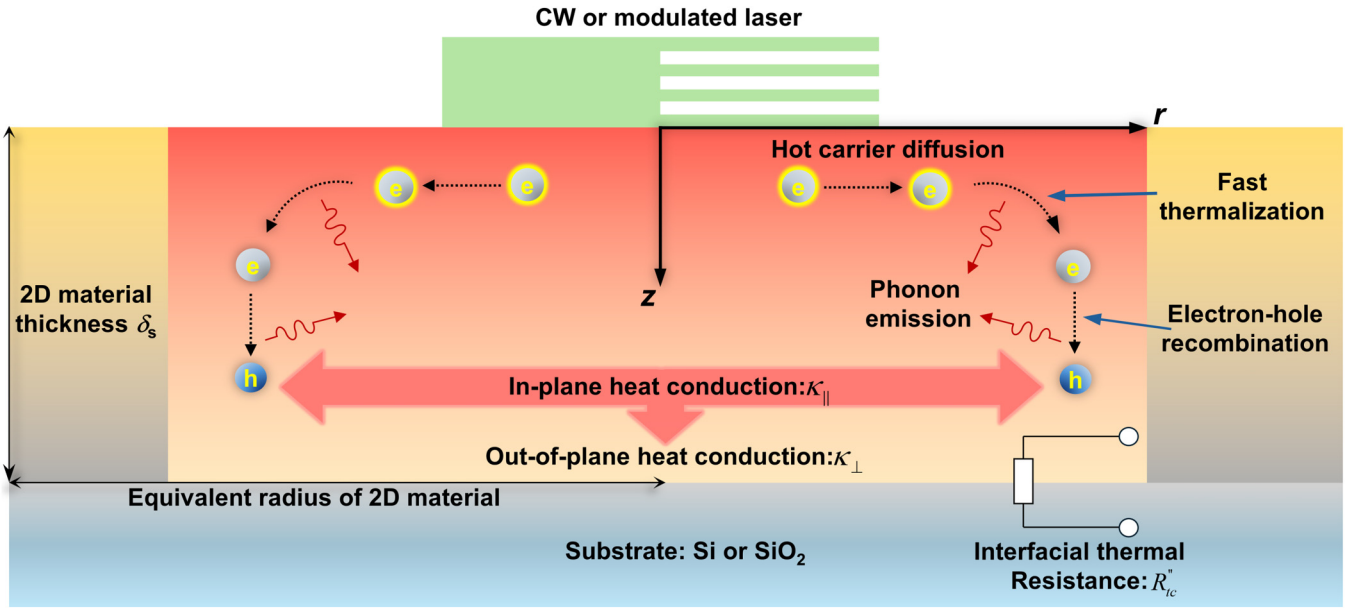

FIG. 5. Schematic of physical processes in FET-Raman measurement of a supported 2D material on a substrate.

optical field distributions in space are the same as they share the same laser source and optical configuration. Heated by different laser power (P), a parameter called Raman shift power coefficient (RSC: ψ) is measured ($\psi = \partial w/\partial P$). It is proportional to the temperature rise of the 2D material. The normalized RSC $\Omega = \psi_{\mathrm{FET}}/\psi_{\mathrm{CW}}$ eliminates the factor of laser absorption and Raman temperature coefficient and can be used to determine R''_{tc}, D, and κ of the 2D material. This technique demonstrates superior accuracy over conventional steady-state Raman approaches and provides a robust platform for characterizing the thermal behaviors of 2D materials.

During data processing of the FET-Raman technique, the computation needs to solve the heat transfer across the interface, within the 2D material, in the substrate, and the hot carrier diffusion in the 2D material. This demands very fine mesh settings and long calculation cycles, which results in very time-consuming analyses, and thus significantly impedes the pace of research and the broader application of this technique. This section demonstrates how this 3D modeling can be conducted using the CFT technique with a dramatic speed increase (>200-fold) while maintaining the same accuracy as the FD method.

In 2D materials, electrically and optically generated hot carriers are crucial for thermal diffusion and heat dissipation.[16] There are three physical processes upon laser heating, which contribute to 2D material's thermal response. As shown in Fig. 5, in the first process, hot carriers are excited by photons. They experience a quick thermalization process (~ps) by releasing the excess energy above the bandgap through non-radiative direct phonon emission (for multi-layered 2D materials). Then, the hot carriers diffuse out of the irradiation area and recombine with holes to release their energy to optical and acoustic phonons. This diffusion process is controlled by the hot carrier diffusivity (D). The second process is the heat conduction in the 2D material, mainly in the in-plane direction, and it is related to the thermal conductivity of 2D materials ($\kappa_{\parallel}$). The third process is the heat conduction from the 2D material to the substrate, which is controlled by the interfacial thermal resistance (R''_{tc}) between them.[7] The generation and diffusion of hot carriers can be described by the following equation:[26]

$$\frac{\partial \Delta N}{\partial t} = D\frac{1}{r}\frac{\partial}{\partial r}\left(r\frac{\partial \Delta N}{\partial r}\right) + \frac{\partial n_0}{\partial T}\frac{\Delta T}{\tau} - \frac{\Delta N}{\tau} + \Phi\alpha. \tag{9}$$

Here, D, τ, and ΔT represent the hot carrier diffusivity, lifetime, and temperature increase, respectively. The first term on the right shows the hot carrier diffusion effect. The term $(\partial n_0/\partial T)\cdot\Delta T/\tau$ is related to thermal activation that generates carriers due to temperature increase. As has been analyzed in our previous research,[27] this term can be neglected because of the moderate temperature rise. n_0 is the equilibrium free-carrier density at a certain temperature T. The term $\Delta N/\tau$ is for the electron-hole recombination. The term $\Phi\alpha$ denotes the hot carrier photo-generation source. α is laser absorptivity. $\Phi = Q/(h\nu)$ (counts $\mathrm{m^{-3}\,s^{-1}}$) (h: Planck constant, ν: photon frequency) is the incident photon flux, and Q ($\mathrm{W\,m^{-3}}$) is the laser power density absorbed in the 2D material, which can be described as

$$Q(r, z, t) = \frac{I_0}{\tau_{\mathrm{L}}}\exp\left(-r^2/r_0^2\right)\exp(-z/\tau_{\mathrm{L}})\Psi. \tag{10}$$

Here, I_0 is the laser intensity in the center of the laser spot without modulation. r_0 is the radius of the laser spot and z is the

location of 2D materials in the thickness direction (shown in Fig. 5). $\tau_L = \lambda/(4\pi k)$ is the laser absorption depth in the 2D material. $\lambda = 532$ nm is the laser wavelength in our modeling. Ψ is the square function modulating the laser with a 50% duty cycle. The heat conduction in the 2D material is governed by phonons and can be described as

$$\rho c_p \frac{\partial \Delta T}{\partial t} = (h\nu - E_g)\Phi\alpha + \kappa_{\parallel}\frac{1}{r}\frac{\partial}{\partial r}\left(r\frac{\partial \Delta T}{\partial r}\right) + \kappa_{\perp}\frac{\partial^2 \Delta T}{\partial z^2} + \frac{\Delta N}{\tau}E_g. \quad (11)$$

On the right side, the first term describes heat generation by the fast hot carrier thermalization process. E_g refers to the bandgap of the 2D material. The second and third terms on the right side are for the in-plane and out-of-plane heat conduction in the 2D material. $\kappa_{\parallel}$ and $\kappa_{\perp}$ refer to the in-plane and out-of-plane thermal conductivity, which arise from the anisotropy of most 2D materials.

In our modeling, a few-layered MoS_2 sample is supported on a Si or SiO_2 substrate. A transmitted laser beam of 1 mW power and 523 nm wavelength is applied. It should be noted that in our modeling, we do not consider the laser absorption characteristics of the substrate since its absorption depth is very long and the heating in the substrate is negligible. The overall computational domain is set up in a cylindrical coordinate to reflect both the radial symmetry of the laser spot and the stratified structure of the sample and substrate. The thickness of the 2D sample (δ_s) is set as 15 nm, and the substrate thickness extends to 30 μm, which serves as a thermal reservoir. The radial domain size for calculation is chosen to be at least 10 times the size of laser spot so that the thermal field near the laser heating area is unaffected by the far-field boundary conditions.

Within this geometry, careful attention is paid on setting the mesh size. In the thickness direction, an extremely fine discretization is required to resolve the sample and the interface region. The smallest grid size in this direction is in the order of a fraction of the 2D sample's thickness, ensuring that the steep temperature gradients across the layer are accurately captured. This fine vertical mesh is also essential for correctly modeling the interfacial thermal resistance, which can strongly influence how heat transfers from the 2D material into the substrate. In the radial direction, the mesh size is chosen to properly resolve the heating area of the Gaussian laser profile, ensuring that the laser intensity distribution at the center of the beam and the gradual decay outward are well represented. By balancing mesh fineness with computational efficiency, the mesh size in the thickness and radial directions are set as 5 and 70 nm, respectively, in the laser spot region within the 2D material. Then, the mesh sizes are gradually increased by a factor of 1.02 from grid to grid in both the radial and thickness directions. Different mesh sizes in the thickness and radial directions have been tested for mesh sensitivity (e.g., 1 and 2 nm in the thickness direction and 30 and 50 nm in the radial direction). They yield very close results as those based on the mesh sizes mentioned above. Since the FD and CFT methods both involve solving the problem in the 3D domain using the finite difference method, iterations are used to solve the equations with a relative convergence criterion of 10^{-6}. We have tried different levels of convergence criterion (down to 10^{-8}) and conclude this one (10^{-6}) is good enough while maintaining reasonable computation cost.

TABLE II. Parameters used in calculation.

Parameters	Values	Units
ρc_p of 2D materials[7]	1.89×10^6	$Jm^{-3}K^{-1}$
Out-of-plane k of 2D materials[7]	2	$Wm^{-1}K^{-1}$
In-plane k of 2D materials[7]	51	$Wm^{-1}K^{-1}$
ρc_p of substrates[28]	1.653×10^6 (Si), 1.659×10^6 (SiO_2)	$Jm^{-3}K^{-1}$
k of substrates	1.38 (SiO_2), 148 (Si)[28]	$Wm^{-1}K^{-1}$
Interfacial thermal resistance[27]	0.5×10^{-6}	Km^2W^{-1}
Mesh size (thickness direction)	5	nm
Mesh size (radial direction)	70	nm
Thickness of the 2D layer	15	nm
Thickness of the substrate	30	μm
Modulation frequency	5–300	MHz
Duty cycle	50	%
Number of heating cycles to calculate	5000	Counts
Electron-hole recombination time[27]	1×10^{-9}	s
The hot carrier's diffusivity[27]	10.2	cm^2/s
Raman laser wavelength	532	nm
The bandgap of the 2D material[29]	1.32	eV

Material properties used in the modeling are summarized in Table II. It is for a MoS_2 layer supported on a substrate (either Si or SiO_2).

To demonstrate the computational accuracy difference of the CFT and FD methods in the spatiotemporal domain, Figs. 6(a) and 6(b) compare the radius–time (r–t) temperature profiles obtained from the FD method and the CFT approach. The calculation target is chosen to be a MoS_2 layer on a SiO_2 substrate. The radius of the laser spot is 0.328 μm, and the modulation frequency of the laser beam is 10 MHz. Under the same radius and time, the ΔT based on the FD method is very close to that of the CFT method. Due to the limitation of time extension for calculation in our FD method, it could not capture the very tiny temperature rise as the heating time approaches infinity. To mediate this effect, we use 5000 cycles of calculation to presume the quasi-steady-state thermal condition can be satisfied. The new CFT method, however, avoids the drawback of calculation time length, clearly captures small increases in sample's temperature rise, and demonstrates superior capability in obtaining the thermal distribution under quasi-steady state of the system.

To illustrate these differences in more specific detail, Fig. 6(c) shows how the temperature of the 2D material surface

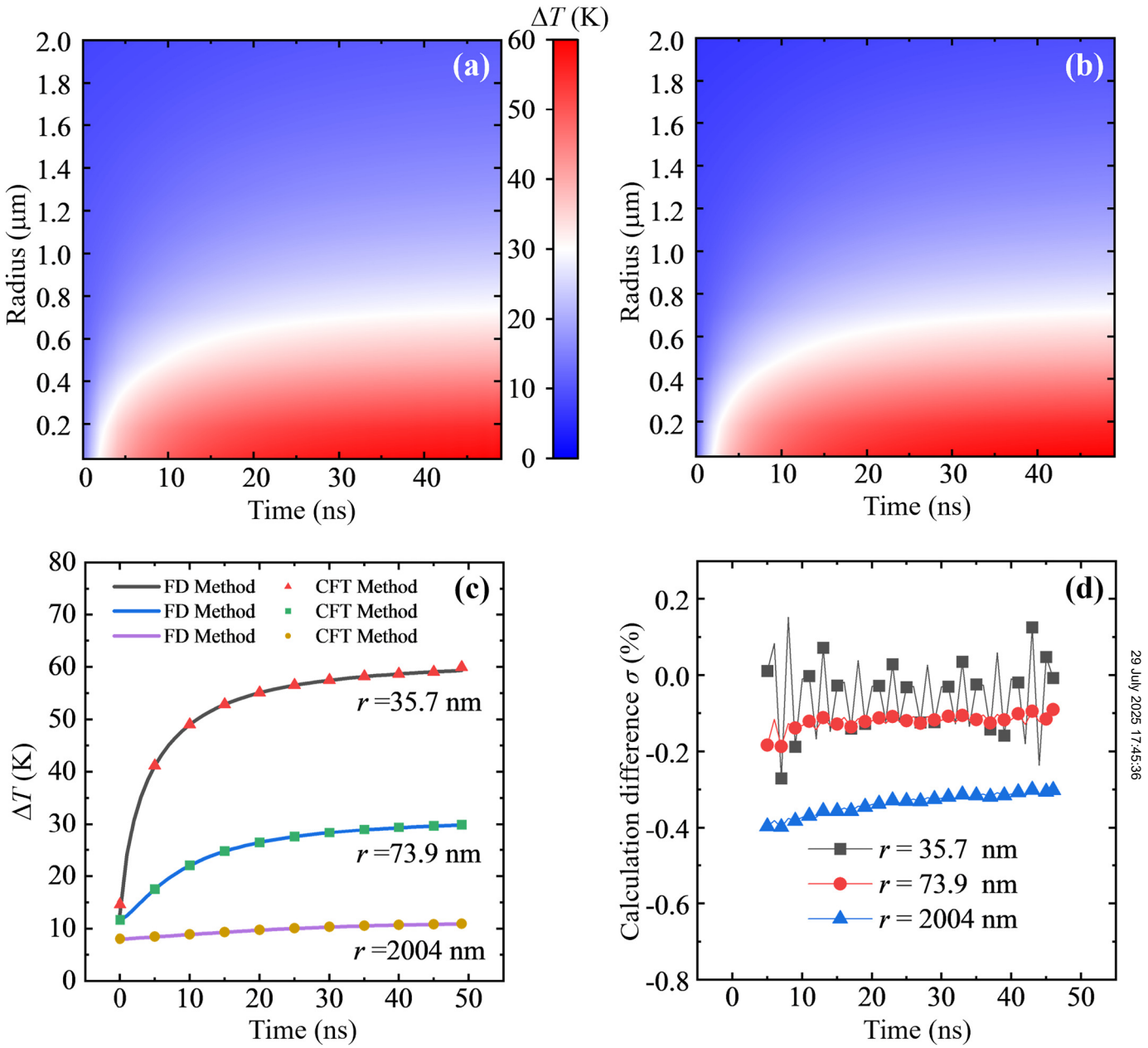

FIG. 6. Radius–time temperature contour for comparison between the (a) CFT and (b) FD method. (c) Temperature changes with time at different radial locations. (d) The relative difference between FD and CFT results.

changes over time at three selected radial positions ($r = 35.7$, 73.9, and 2004 nm). Using the FD method, the temperature at these points appears slightly different at the very beginning of the laser heating process when the heating time is smaller than 10 ns. This could be due to the oscillation in the reconstructed square laser pulse using 40 Fourier terms. As the heating time increases, the ΔT by the FD and CFT methods are highly aligned. The comparison of temperature rise is further quantified in Fig. 6(d). Here, the calculation difference σ between them is defined as $\sigma = (\Delta T_{FD} - \Delta T_{CFT})/\Delta T_{CFT}$. The difference is no more than 1%, showing the CFT method is highly aligned with the classical FD method.

It is worth noting that the CFT method greatly improves computational efficiency and accuracy. Here, we evaluated the calculation duration time of the two methods. All numerical simulations and data processing are performed on a Dell Precision T1700 PC. This system is equipped with an Intel Core i7-4790 CPU, with 16 GB of DDR3 RAM running at 1600 MHz. Data storage and program execution utilize a 256 GB solid-state drive. The simulations are conducted under Windows 10. The FD approach requires solving the heat conduction equation at every time step. In the FD method, the time step is 5.57×10^{-14} s based on the very fine mesh setting. The total time to calculate the heat transfer in the sample to reach the quasi-steady state should be at least 50 ns. The number of calculation steps to solve the heat conduction equation is about $50 \times 10^{-9}/5.57 \times 10^{-14} = 897\,666$. However, our CFT approach can achieve comparable accuracy with a significantly reduced number of steps. For instance, the CFT method transforms the heat conduction equation into 40 steady-state ones in the complex domain, which means that the heat conduction equation is solved only 40 times in total, rather than 897 666 times. This represents more than four orders of magnitude reduction in computational time. On the other hand, solving the transformed heat conduction equation in the complex domain takes a little more time than the normal steady-state heat conduction equation. Our real case computation shows that using the FD method, it takes about 10 h or more for computing the temperature evolution over 500 μs, while the CFT method only takes about 3 min to finish. This firmly proves the CFT method can reduce the computational time by 2–3 orders of magnitude or more. For the FD computation, we also tried using COMSOL on a computer equipped with an Intel(R) Xeon(R) Gold 6248R CPU at 3.00 GHz, NVIDIA Quadro RTX5000 16 GB, and 512 GB memory at 3200 MHz. Under 25 MHz laser heating, for a heating time of 250 μs, it takes about 10 h to finish, while for such case our lab-developed FD solver only takes about 5 h. It should be noted the speed increase by the CFD method vs FD is based on the same platform of FD solver and computer hardware. If a different solver and computer hardware platform are used, the same speed increase still holds true.

The modulation frequency (f) of the laser plays a crucial role in shaping the sample's thermal response. Here, the temperature response of the sample is modeled using the CFT method under different modulation frequencies when different objectives are used. The laser spot under different objectives is given in Table III. Table III also shows the calculated temperature rise of the sample under CW laser irradiation. Note this temperature rise controls ψ in FET-Raman and is a Raman intensity-weighted value. It is calculated as

$$\Delta T_{\mathrm{CW}} = \int_0^V Ie^{-z/\tau_{\mathrm{L}}} \Delta T dv / \int_0^V Ie^{-z/\tau_{\mathrm{L}}} dv, \tag{12}$$

$$\Delta T_{\mathrm{FET}} = \int_0^t \int_0^V Ie^{-z/\tau_{\mathrm{L}}} \Delta T dv dt / \int_0^t \int_0^V Ie^{-z/\tau_{\mathrm{L}}} dv dt, \tag{13}$$

where $I = I_0 \exp(-r^2/r_0^2)\exp(z/\tau_{\mathrm{L}})$. ΔT is the material temperature rise. z is the distance from the 2D material's upper surface (Fig. 5).

Figure 7 shows the temperature rise varies with $1/f$ for MoS_2 supported on Si and SiO_2. It is observed that the temperature rise decreases with increased modulation frequency from 5 to 300 MHz. At lower frequencies, each pulse lasts longer, allowing more time for heat to build up. So the temperature rise of the sample under the transient state is closer to the temperature rise under CW laser heating when f is very low. As the frequency increases, the sample receives power in shorter bursts, leaving less time for the temperature to climb significantly within each cycle. The fluctuation of temperature rises becomes smaller. In the limit of extremely high frequencies, the variation of temperature in one heating period approaches zero and ΔT converges to half of the CW case as shown in Fig. 7. Considering the total heating power input (E_f) in the FET-Raman case is equal to half of CW case (E_{cw}), at very high f, the heat transfer in 2D materials under FET cases is similar as a CW case with half energy input (0.5 E_{cw}).

To comprehensively compare the difference between the CFT and FD results, we calculate the difference of Raman intensity-weighted temperature rise (ΔT) of the 15 nm-thick MoS_2 supported on the SiO_2 substrate for various laser spot radii and laser modulation frequencies. As shown in Fig. 8, the calculation difference between the two methods is bigger under higher modulation frequencies. However, this increase in discrepancy is due to the computational time limit in the FD method, not the calculation uncertainty of the CFT method. In all calculation cases using the FD method, we use the same 5000 heating cycles. This leads to a shorter calculation time for higher modulation frequency cases. This means the sample is further from reaching the quasi-steady state for these cases, so the temperature rise calculated using the FD method is lower than the value by the CFT method. So here the CFT method provides much more accurate modeling results.

TABLE III. Steady-state temperature rise (ΔT) of the sample under CW laser irradiation.

Object lens	Laser spot radius r_0 (μm)	ΔT of MoS_2 on Si (K)	ΔT of MoS_2 on SiO_2 (K)
20×	1.400	8.20	26.26
50×	0.526	24.43	49.29
100×	0.328	35.66	62.22

V. EXTENSION TO HEAT TRANSFER WITH ARBITRARY TRANSIENT HEAT SOURCE: HEAVISIDE TRANSFORM

For the heat transfer problem described by Eq. (1), the heat source has a distribution in space, but follows the same manner of variation with time ($\dot{q}$). For a generalized situation where there are several distributed heat sources, each one with a specific spatial distribution and time variation (but with the same frequency f) as

$$\rho c_p \frac{\partial T}{\partial t} = \kappa \nabla^2 T + \sum_{i=1}^{n} g_i(\vec{r}) \cdot \dot{q}_i. \tag{14}$$

The temperature field T_i induced by each heat source $g_i(\vec{r}) \cdot \dot{q}_i$ can be solved numerically using the CFT method described in

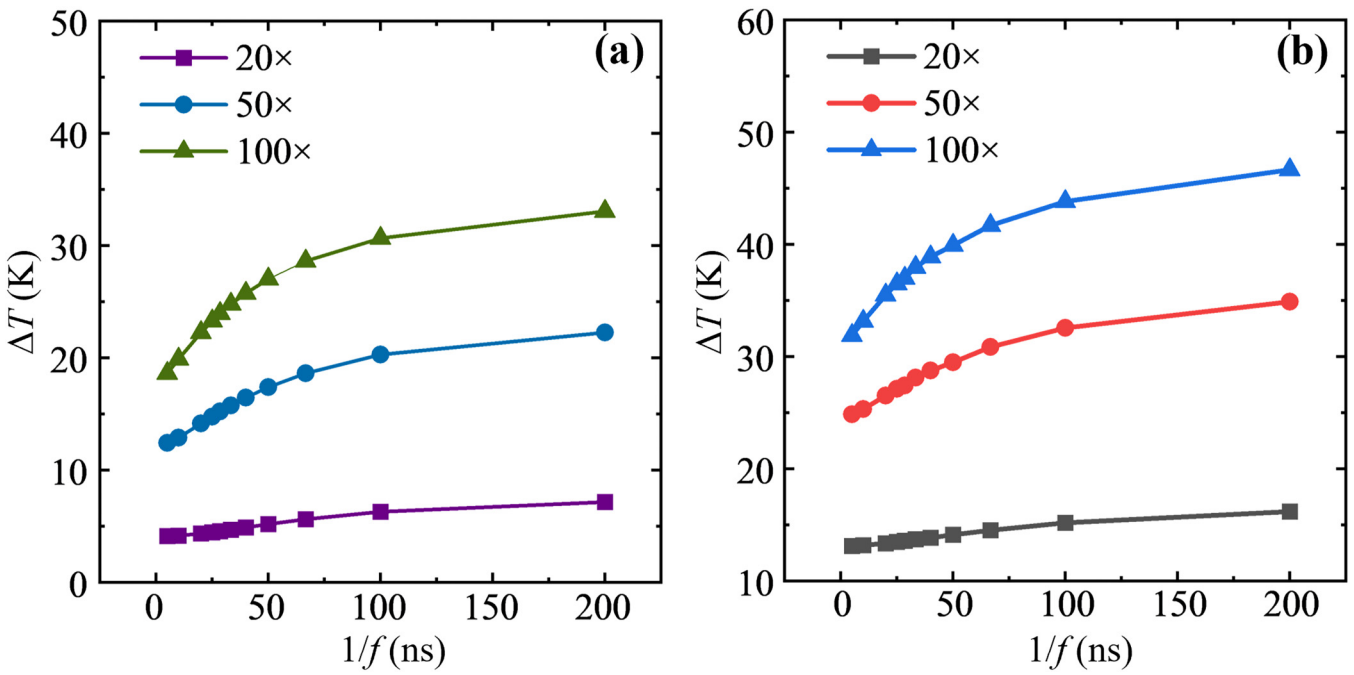

FIG. 7. Variation of temperature rise 1/*f* calculated using the CFT method on different substrates: (a) Si and (b) SiO_2.

Sec. II, and then the overall temperature can be expressed as $T = \sum_{i=1}^{n} T_i$.

For a transient heat transfer problem with a heat source of arbitrary, non-periodical variation with time $g(\vec{r}) \cdot \dot{q}$, we present a method based on the CFT method above, termed Complex-modeling with Fourier and Heaviside Transform (CFHT). Here, $g(\vec{r})$ describes the heat source spatial distribution, and $\dot{q}$ varies with time following the same way for all locations, as illustrated in Fig. 9. Mathematically, $\dot{q}$ can be expressed as a sum of Heaviside step functions as[30]

$$\dot{q}(t) = \sum_{i=1}^{\infty} [\dot{q}(i \cdot \Delta t) - \dot{q}((i-1) \cdot \Delta t)] \cdot h(i \cdot \Delta t, t). \quad (15)$$

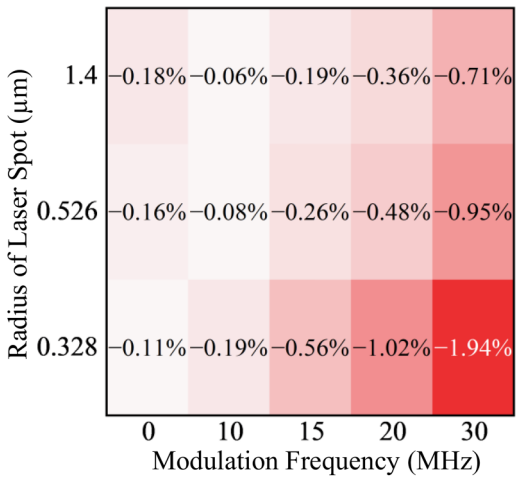

FIG. 8. Comparison between FD and CFT methods for different laser spot radii and modulation frequencies.

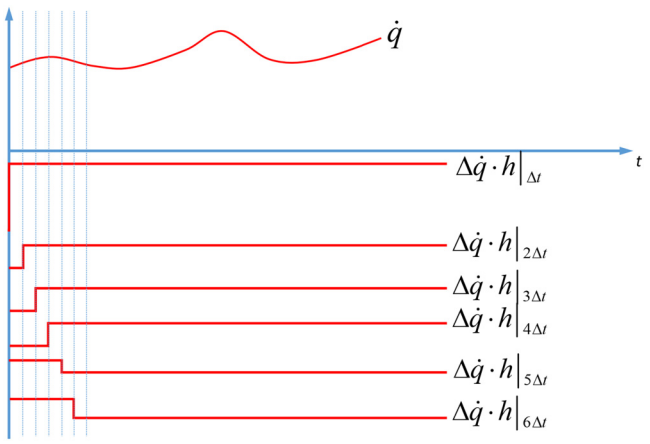

FIG. 9. Schematic of the Heaviside transform to reconstruct the arbitrary time-varying $\dot{q}$.

Here, the Heaviside step function $h(\tau, t)$ is expressed as

$$h(\tau, t) = \begin{cases} 0 & (t < \tau) \\ 1 & (t \geq \tau). \end{cases} \tag{16}$$

Figure 9 shows the schematic of this Heaviside step function transform, with

$$\Delta\dot{q} \cdot h|_{i\Delta t} = [\dot{q}(i \cdot \Delta t) - \dot{q}((i-1) \cdot \Delta t)] \cdot h(i \cdot \Delta t, t). \tag{17}$$

For a heat transfer problem with a heat source of $g_i(\vec{r}) \cdot h(0, t)$, this represents a step function heat source problem. Traditionally, this problem needs to be solved step by step using the finite difference or element method until it reaches the steady state.

Here, we show that it can also be solved using the CFT method very efficiently. First, we reconstruct a heat transfer problem with a periodical square-wave heat source $g(\vec{r}) \cdot \Psi$ whose frequency is f. For this square wave Ψ, we set its duty time $[t_0 = 1/(2f)]$ sufficiently long, so during one duty, the system will reach the steady state. Ψ is 1 during the duty, and 0 out of duty. The temperature field T_Ψ induced by $g(\vec{r}) \cdot \Psi$ can be readily solved using the CFT method described in Sec. II. Then for a problem with a heat source of $g_i(\vec{r}) \cdot h(0, t)$, its solution is

$$T_h(t) = \begin{cases} T_\Psi(t) & (t \leq t_0) \\ T_\Psi(t_0) & (t > t_0). \end{cases} \tag{18}$$

Finally, the temperature field induced by a general arbitrary time-varying heat source $g(\vec{r}) \cdot \dot{q}$ can be simply reconstructed as

$$T(t) = \sum_{i=1}^{N} [\dot{q}(i \cdot \Delta t) - \dot{q}((i-1) \cdot \Delta t)] \cdot T_h[(N-i)\Delta t], \quad (N = t/Dt). \tag{19}$$

For this transient problem, numerical modeling is only needed to solve the temperature field T_Ψ that is induced by $g(\vec{r}) \cdot \Psi$, and this can be done one time using the CFT method. We expect the computational time will be reduced by several orders of magnitude compared with the classical step-forwarding finite methods.

To demonstrate the effectiveness and computational efficiency of the proposed CFHT method, we study a transient heat transfer case of the same configuration studied in the above section. The laser spot radius is 0.328 μm, the 2D material is 15 nm thick MoS_2, and the substrate is SiO_2. The temporal variation of the laser is defined as a triangular wave of 500 μs duration and a peak power of 1 mW at 250 μs. Within the heating time, the heating intensity linearly increases from 0 to 1 mW over the first 250 μs, followed by a symmetric linear decrease back to 0 over the next 250 μs. All the other parameters used in this simulation are the same as listed in Table II. Using the CFHT method, this time-dependent heat source is decomposed into a series of Heaviside step functions with an interval of $\Delta t = 10\,\mu$s, whose temperature response is computed using the CFT method. In the CFT computation, only 40 Fourier terms are used, and a square-wave heating source of 2000 Hz is used to construct the thermal response of a Heaviside step function.

Figure 10(a) presents the contour map of the resulting temperature of the 2D material surface calculated using the CFHT method. The magnitude of the temperature diminishes with increased radial distance, consistent with diffusive heat spreading from the laser heating center. To further validate the accuracy of the CFHT method, we compare the temperature profile at a certain radius with that calculated using the FD method. Figure 10(b) shows the temporal evolution of the temperature at a fixed radius of 35.7 nm, as computed by both the CFHT and FD approaches. Also, we evaluate the difference between the two methods $\sigma = T_{\mathrm{CFHT}} - T_{\mathrm{FD}}$. The results show high agreement between the two methods, in which the maximum difference is less than 1 K, confirming the high fidelity of the CFHT reconstruction.

Notably, the temperature response in Fig. 10(b) shows a triangular shape that closely follows the temporal profile of the heat source. This behavior can be physically explained by analyzing the thermal response characteristics of each Heaviside step function used in the CFHT method. For each incremental step in the decomposition of the triangular heat source, the thermal response can be considered the system's reaction to a sudden onset of localized heating. In our model, the thermal resistance of the interface between the substrate and the 2D material (R_{int}), and the thermal resistance of the substrate (R_{sub}) can be evaluated as $R_{\mathrm{int}} = R''_{tc}/(\pi \cdot r_0^2)$ and $R_{\mathrm{sub}} = 1/(4k_{\mathrm{sub}} \cdot r_0)$, where r_0 is the laser spot radius and k_{sub} is the substrate's thermal conductivity. The ratio of temperature rise induced by R_{int} (T_{int}) to the total temperature rise (T_{total}) and the buildup time of this part can be evaluated based on the following relations $T_{\mathrm{int}}/T_{\mathrm{total}} \propto R_{\mathrm{int}}/(R_{\mathrm{int}} + R_{\mathrm{sub}})t_{\mathrm{int}} = \Delta z \cdot \rho c_p \cdot R''_{tc}$ (Δz is the 2D material thickness and ρc_p is for the 2D material). According to the used parameters, R_{int} is 1.48×10^6 K/W, R_{sub} is 5.44×10^5 K/W, $T_{\mathrm{int}}/T_{\mathrm{total}}$ is 73%, and t_{int} is 14 ns. Due to the small laser spot radius, R_{int} dominates the total thermal resistance: $R_{\mathrm{int}} + R_{\mathrm{sub}}$. As a result, in the first 14 ns in the heating step, the temperature rise at the 2D material surface quickly reaches ~73% of the total temperature rise, primarily reflecting the rapid increase in the temperature difference between the 2D material and substrate. Following this rapid initial rise, the temperature increases more gradually as the heat continues to diffuse into the substrate. This two-step behavior makes the temperature response of each Heaviside step resembles a step-like function. When these individual step responses are superimposed in time, they reconstruct a triangular temperature rise. Thus, the triangular shape observed in the temperature profile is not simply a direct response to the triangular power input, but rather an emergent feature resulting from the accumulation of multiple asymmetric, step-like thermal responses weighted over time. However, if the thermal response to each Heaviside step is more gradual, the overall temperature profile would no longer be triangular, but rather an asymmetric bell-like or trapezoidal profile. A good example is the case with a thicker 2D material, where the temporal evolution of temperature under each Heaviside step input would exhibit a slower rise, possibly resembling an exponential or sigmoidal curve. Therefore, the final temperature profile reconstructed by the CFHT method is not only determined by the shape of the power input alone, but rather by the combination of the input waveform and the system's thermal property, illustrating the critical

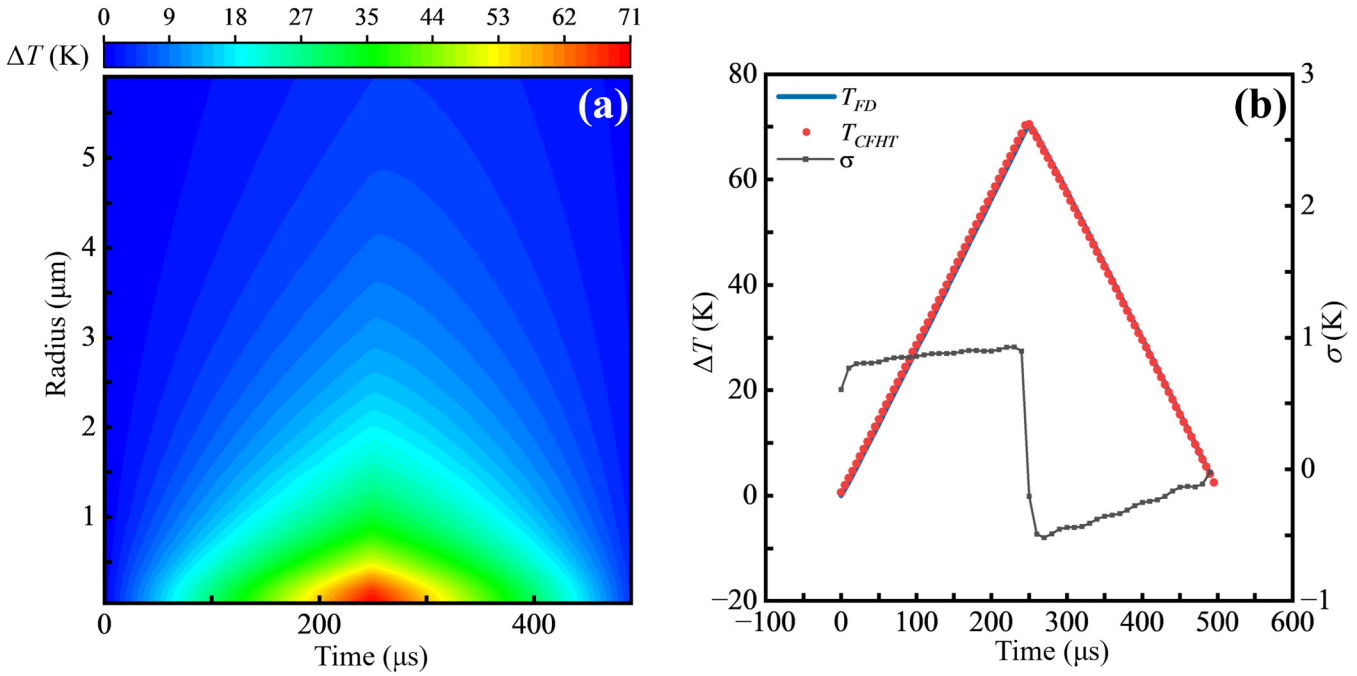

FIG. 10. (a) The contour map showing the relation between the temperature profile and the radius from heating center and heating time based on CFHT calculation. (b) The temperature response at the radius of 35.7 nm by the CFHT and the FD methods and their difference.

role that material properties and interfacial effects play an important role in determining the observed transient thermal behavior.

The CFHT method not only reproduces the spatiotemporal temperature field with high accuracy but also achieves significant computational acceleration. In this triangle heating case, the CFHT method reduces the simulation time from 10 h (by FD) to under 3 min (by CFHT) on the PC platform mentioned before. It should be noted that for simulations of longer time scales, the advantage of the CFHT method will be further expanded. For example, for the case studied here, if the arbitrary heating time is 1 ms, the computation will take about 20 h based on the FD method. However, in the CFHT method, we still only need to make 40 calculations in CFT, which will consume the same 3 min as the case shown, and then reconstruct the thermal response under real heating that can be finished in a very short time (seconds). What is more, we can apply a smaller Δt at a cost of negligible computation cost increase to effectively improve the time accuracy of the calculation results in CFHT.

For the CFT and CFHT methods described in this work, although they are presented for linear heat transfer problems, eventually they are applicable to all linear problems. Examples include linear mechanics problems under various external excitation (thermal, mechanical, laser, etc.).[31] However, for nonlinear problems, for example, heat transfer problems involving strong temperature-dependent thermophysical properties,[32] both CFT and CFHT methods cannot be used since the physics decomposition described in Sec. II cannot be applied. Under such scenarios, the traditional finite element methods are still applicable and more effective. However, for such scenarios, averaged temperature-dependent thermophysical properties can be assumed to provide first-order estimation of the problem using the CFT and CFHT methods. For problems of periodical external excitation (thermal, mechanical, and photon), as we have demonstrated above, if the excitation is square waves of 50% duty, 40 Fourier terms are sufficient for the CFT method. However, if the duty is smaller, e.g., 10%, more Fourier terms are needed to capture the fine system response during the short excitation duration. The needed number of Fourier terms should be chosen so that the reconstructed excitation using Eq. (2) well reflects the real one.

VI. CONCLUSION

In this work, we developed the CFT technique that solves quasi-steady-state energy transport problems with a periodically time-varying heat source. The CFT method decomposes the transient energy transport problem into problems with a complex-temperature response. These problems can be solved just one time, and their resolutions are used to construct the resolution to the real physical energy transport problem. The CFT method was demonstrated by solving two typical problems. One is a supported SWCNT bundle under periodical laser heating and the energy transport inside involves heat conduction and interfacial energy transport. The other one is a nm-thick 2D material supported on a substrate. Its thermal behavior involves 3D phonon transport, hot

carrier diffusion, and interfacial energy transport. It was confirmed that the CFT method yielded a similar level or higher accuracy compared with the FD method, while the CFT method features a speed of more than two orders of magnitude faster than the FD method. Furthermore, a general method, termed CFHT, was developed that can solve any transient energy transport problems, with orders of magnitude increase in computational speed. The developed CFT and CFHT techniques are applicable to linear problems that involve transient heat sources.

ACKNOWLEDGMENTS

Partial support of this work by the U.S. National Science Foundation (X.W., CMMI 2032464 and CBET 2425361) and General Program for Basic Research-Shenzhen Municipal Science, Technology and Innovation Commission (Y.X., JCYJ20240813142120027) is gratefully acknowledged.

AUTHOR DECLARATIONS

Conflict of Interest

The authors have no conflicts to disclose.

Author Contributions

Yu Hua: Data curation (equal); Formal analysis (equal); Investigation (equal); Validation (equal); Writing – original draft (equal). **Ibrahim Al Keyyam:** Data curation (equal); Formal analysis (equal); Investigation (equal); Validation (equal); Writing – original draft (equal). **Yangsu Xie:** Conceptualization (supporting); Data curation (supporting); Investigation (supporting); Methodology (supporting); Writing – review & editing (supporting). **Xinwei Wang:** Conceptualization (lead); Funding acquisition (lead); Investigation (lead); Methodology (lead); Project administration (lead); Software (lead); Supervision (lead); Writing – original draft (lead); Writing – review & editing (lead).

DATA AVAILABILITY

The data that support the findings of this study are available from the corresponding author upon reasonable request.

REFERENCES

[1]J. Liu, M. Han, R. Wang, S. Xu, and X. Wang, J. Appl. Phys. **131**, 065107 (2022).
[2]X. Wang, B. A. Cola, T. Bougher, S. L. Hodson, T. S. Fisher, and X. Xu, Annu. Rev. Heat Transfer **16**, 135 (2013).
[3]T. Wang, X. Wang, Y. Zhang, L. Liu, L. Xu, Y. Liu, L. Zhang, Z. Luo, and K. Cen, J. Appl. Phys. **104**, 013528 (2008).
[4]X. Wang, H. Hu, and X. Xu, J. Heat Transfer **123**, 138 (2001).
[5]H. Hu, X. Wang, and X. Xu, J. Appl. Phys. **86**, 3953 (1999).
[6]K. D. Cole and W. A. Mcgahan, J. Heat Transfer **115**, 767 (1993).
[7]P. Yuan, R. Wang, H. Tan, T. Wang, and X. Wang, ACS Photonics **4**, 3115 (2017).
[8]H. Zobeiri, R. Wang, T. Wang, H. Lin, C. Deng, and X. Wang, Int. J. Heat Mass Transfer **133**, 1074 (2019).
[9]R. Wang, H. Zobeiri, H. Lin, W. Qu, X. Bai, C. Deng, and X. Wang, Carbon **147**, 58 (2019).
[10]X. Guo, S. Cheng, W. Cai, Y. Zhang, and X. Zhang, Mater. Des. **209**, 109936 (2021).
[11]B. Kumanek and D. Janas, J. Mater. Sci. **54**, 7397 (2019).
[12]I. Al Keyyam, B. Li, T. Wang, C. Deng, and X. Wang, Carbon **233**, 119906 (2025).
[13]I. Al Keyyam, M. Rahbar, N. Hunter, B. Li, T. Wang, E. Shi, and X. Wang, Int. J. Heat Mass Transfer **226**, 125513 (2024).
[14]I. Al Keyyam, M. Rahbar, E. Shi, B. Li, T. Wang, and X. Wang, J. Phys. Chem. C **128**, 1505 (2024).
[15]I. Al Keyyam and X. Wang, Mater. Today Phys. **46**, 101516 (2024).
[16]M. Rahbar, B. Li, N. Hunter, I. Al Keyyam, T. Wang, E. Shi, and X. Wang, Cell Rep. Phys. Sci. **4**, 101688 (2023).
[17]Y. Feng, T. Inoue, H. An, R. Xiang, S. Chiashi, and S. Maruyama, Appl. Phys. Lett. **112**, 191904 (2018).
[18]J. R. Lukes and H. Zhong, J. Heat Transfer **129**, 705 (2007).
[19]L. Shi, J. Zhou, P. Kim, A. Bachtold, A. Majumdar, and P. L. McEuen, J. Appl. Phys. **105**, 104306 (2009).
[20]J. Hone, B. Batlogg, Z. Benes, A. T. Johnson, and J. E. Fischer, Science **289**, 1730 (2000).
[21]T. Wang, S. Xu, D. H. Hurley, Y. Yue, and X. Wang, Opt. Lett. **41**, 80 (2016).
[22]A. A. Balandin, Nat. Mater. **10**, 569 (2011).
[23]L. M. Uriarte, L. J. Bonales, J. C. Dubessy, Á Lobato, V. G. Baonza, and M. Cáceres, Microchem. J. **139**, 134 (2018).
[24]S. Xu, A. Fan, H. Wang, X. Zhang, and X. Wang, Int. J. Heat Mass Transfer **154**, 119751 (2020).
[25]Z. Deng, J. Cai, G. Wang, and J. Liu, Int. J. Heat Mass Transfer **230**, 125810 (2024).
[26]M. Nestoros, B. C. Forget, C. Christofides, and A. Seas, Phys. Rev. B **51**, 14115 (1995).
[27]P. Yuan, H. Tan, R. Wang, T. Wang, and X. Wang, RSC Adv. **8**, 12767 (2018).
[28]T. L. Bergman, *Fundamentals of Heat and Mass Transfer*, 7th ed. (John Wiley & Sons, 2011).
[29]P. Yuan, C. Li, S. Xu, J. Liu, and X. Wang, Acta Mater. **122**, 152 (2017).
[30]A. Karamati, S. Xu, H. Lin, M. Rahbar, and X. Wang, JUSTC **53**, 1001 (2023).
[31]Y. He, S. Wan, S. Zhou, Z. Huang, Y. Chang, Y. Yang, X. Gao, Y. Xu, J. Yang, S. Gao, D. Ma, Y. Zhou, and H. Sun, Appl. Phys. Lett. **126**, 122201 (2025).
[32]H. Yang, R. Hu, H. Wu, X. He, Y. Zhou, Y. Xue, K. He, W. Hu, H. Chen, M. Gong, X. Zhang, P.-H. Tan, E. R. Hernández, and Y. Xie, Nano Lett. **24**, 2789 (2024).